NANO LETTERS

2008
Vol. 8, No. 2
516−519

Metallic Glass Nanowire

Koji S. Nakayama,* Y. Yokoyama, G. Xie, Q. S. Zhang, M. W. Chen, T. Sakurai, and A. Inoue

Institute for Materials Research, Tohoku University, Sendai 980-8577, Japan

Received October 23, 2007

ABSTRACT

Metallic glass nanowires were spontaneously created on the fracture surfaces that were produced by a conventional mechanical test. The presence of the nanowires is directly related to the one-dimensional meniscus configuration with a small viscosity at high temperatures and to the wide supercooled liquid region of the metallic glass. The electron microscopic observations demonstrate the diameters, the lengths, and the amorphous structural states, and the energy dispersive X-ray reveals the chemical components. In addition, we found that round ridges are constructed from nanotubes. The finding of amorphous nanostructures not only provides a fundamental understanding of fracture processes but also gives a new insight into nanoengineering constructions.

Nanostructures such as nanowires and nanotubes are the essential backbone to construct nanoscale devices.[1−5] The functionality of such small devices is closely related to the mechanical properties that are determined by interatomic bonding strength and structural disordered/ordered configurations. While the previously discovered nanostructures are mainly composed of crystalline states,[6,7] theoretical studies have predicted that the amorphous state is favorable for metallic nanowires with structural stability.[8−10] In this Letter, we report the metallic glass nanowire and nanotube that are constructed from a Zr-based bulk metallic glass (BMG). The characterization of these nanostructures provides a fundamental understanding of BMG destruction processes and has important implications for nanoelectromechanical systems.

The materials of BMG received attention because they offer unique mechanical properties such as ultrahigh strength, high hardness, and large elastic strain due to the absence of a crystal slip.[11−13] There have been extensive studies regarding the mechanical behavior of the BMGs that is associated with the nanoscale structural evolution including the dynamic crack propagation,[14] the nanocrystallization along shear bands,[15] and the microstructure formation.[16] However, far less attention has been paid to the formation of the metallic glass nanostructures though they are expected to inherit the superior mechanical properties. Nevertheless, the metallic amorphous or glassy nanowires have not been achieved experimentally, in particular, those formed by mechanical processes during fracture. The observations of a scanning electron microscope (SEM) demonstrate that the nanowires, ranging from 10 nm to ∼1 μm in diameter and ∼50 μm in length, appear on the fracture surfaces, which were prepared by a conventional compressive test. Figure 1 illustrates the uniaxial compressive test for a cylindrical BMG sample.

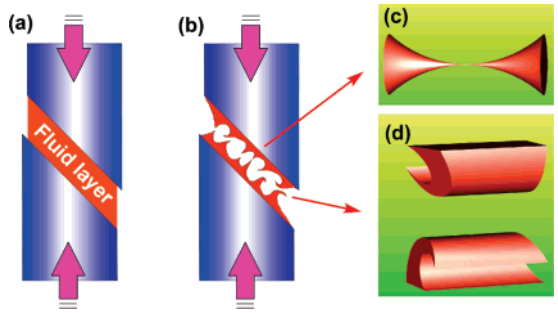

Figure 1. (a) Illustrations of a conventional compressive test. The shear localization causes a rapid temperature rise, and the adiabatic heating induced the formation of a fluid layer. (b) The nucleation of nano/microvoids and the rupture of the fluid layer occur at the final stage. (c) One-dimensional meniscus leads to a wire formation. (d) The disruption of two-dimensional meniscus causes a tubular shape.

Compressive deformation leads to the localized plastic flow and the shear band formation.[17−19] The localization causes a rapid temperature increase while the adiabatic heating results in extremely fast events within a few hundred nanoseconds.[20] Such a substantial increase in temperature in the narrow shear band induces the formation of a fluid layer, as illustrated in Figure 1a. The nano/microvoids are created in the layer, and the rupture occurs at the final stage in Figure 1b. The rapid cooling of viscous fluid layers leads to the formation of well-known "*vein patterns*", as reported in the previous fractographic studies.[12,17−20] The energy dispersive X-ray (EDX) was performed to identify chemical components on the fracture surfaces, and a conventional transmission electron microscope (TEM) technique was used to verify structural states of the nanowire. Furthermore, the cross-sectional view for the vein ridges prepared by an ion milling provided that the ridges are constructed from a tubular structure, indicating the presence of nanotubes.

* To whom correspondence should be addressed: kojisn@imr.tohoku.ac.jp.

10.1021/nl0727462 CCC: $40.75
Published on Web 01/15/2008

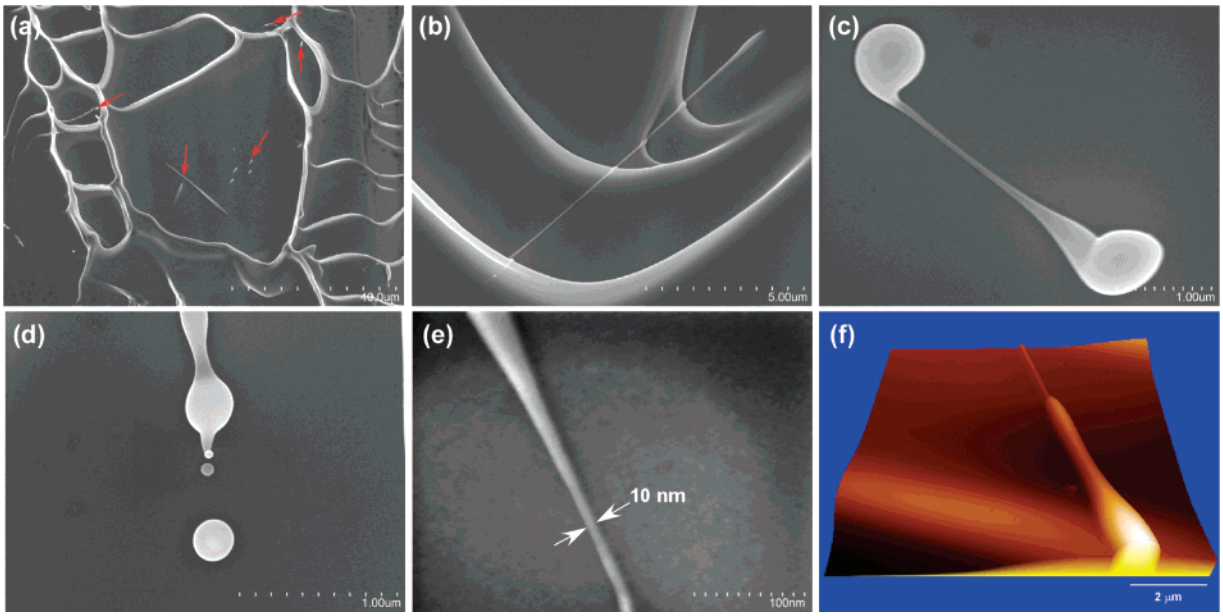

Figure 2. (a) Field emission SEM image of a vein pattern. Red arrows indicate nanostructures. (b) The nanowire having 12 μm in length appears on the vein. (c) A gourd-shaped nanowire has a droplet at each end. (d) Spherical drops appear near the top of the nanowire. (e) High-resolution SEM image shows the 10 nm diameter nanowire. (f) The AFM image represents the three-dimensional feature of the nanowire. For this nanowire, the smaller diameter is 130 nm and the larger diameter is 420 nm.

We used the $Zr_{50}Cu_{40}Al_{10}$ BMG that exhibits a high glass-forming ability, a wide supercooled liquid region, and superior mechanical properties such as the tensile strength of 1860 MPa, the Young's modulus of 89 GPa, and the Vickers hardness of 506.[21] To produce BMG, we used a ternary Zr−Cu−Al alloy that was melted with a mixture of pure Zr, Cu, and Al metals in an argon atmosphere. To minimize oxygen concentration during the BMG production, we used the Zr crystal rods that contained less than 0.05 atomic % of oxygen. We employed a tilt casting technique that has an advantage of preventing cold spots during solidification.[21] The melting alloy was cast into a rod-shaped mold that has the size of 3 mm in diameter and ~60 mm in length. To obtain the fracture surface, the sample was cut by a diamond saw about 5 mm in length, and the compressive test was performed in air with an average strain rate of 5×10^{-4} s^{-1}. The fracture surfaces were observed by a field emission SEM (Hitachi S-4800 operated at 15 kV), atomic force microscope (AFM) (JEOL JSPM-5400), and TEM (JEOL JEM-2010 operated at 200 keV). The EDX system (EDAX Genesis XM2H) was combined with the SEM. We used two ion milling systems for sample preparation. One was the focused ion beam (FIB) system (Hitachi FB-2100) with 40 keV Ga ion beam, and the other was the Ar ion milling system (Hitachi E-3500) at 6 keV. The latter equipped a Ti shield plate in front of the sample, and the uncovered area from the shield was able be removed by the irradiation with the low-energy ion, as depicted in Figure 5a. Such a configuration allowed us to visualize cross-sectional features of the vein ridge structures.

Figure 2a represents the SEM image of the fracture surface of the $Zr_{50}Cu_{40}Al_{10}$ BMG. The morphology-like cellular "vein pattern" consists of a network of round ridges. The red arrows indicate nanostructures that can be recognized even in the low magnification SEM image. The image in Figure 2b shows a nanowire that has 12 μm length and lies across four steps on the vein pattern. Although fracture processes are complicated, the existence of the nanowire on the vein pattern implies different formation pathways between nanowire and vein. The local viscosity is significantly lowered, and a liquid bridge is created in the final stage. The one-dimensional meniscus configuration allows extending the viscous molten that results in wire formation, as depicted in Figure 1c. In contrast, the two-dimensional meniscus configuration originates a round ridge on a fracture surface, as illustrated in Figure 1d. In the latter case, we can expect that some ridges contain a tubular structure, as discussed below. For the nanowire formation, the local viscosity and the stretching period control the structural shapes. For example, the limited stretching time produces a gourd-shaped nanowire having a droplet at each end, as shown in Figure 2c. When the local viscosity is extremely lowered, the spherical shape that minimizes the surface tension can be formed. Figure 2d shows two spherical drops that have 80 and 250 nm in diameter, respectively. Most importantly, the highest resolution SEM image in Figure 2e demonstrates the nanowire that has the smallest diameter of 10 nm in our observations. Figure 2f is an AFM image that can provide geometrical profiles having atomically smooth surface features. For this nanowire, the smallest diameter is 130 nm and the largest diameter is 420 nm. The thinner part is extended to more than 3 μm, and the thicker part lies on a vein step. The bottom of the nanowire does not show its actual profile because the access of the AFM cantilever was limited.

Both SEM and AFM represented an atomically smooth surface morphology on nanowires that would be attributed to an amorphous nature. Such a structural phase is very

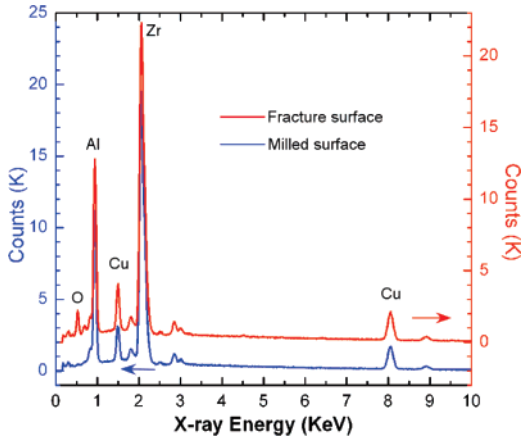

Figure 3. The averaged EDX spectra were obtained from the milled surface and the fracture surface of Figure 5b.

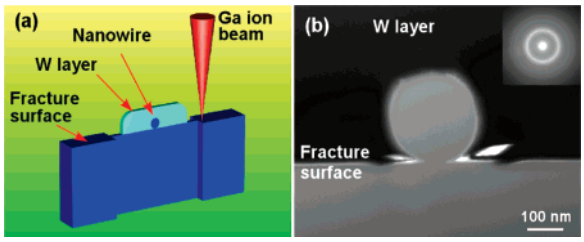

Figure 4. (a) Illustration during FIB fabrication for a nanowire. (b) The TEM image represents the cross section of the nanowire. The image reveals its structural uniformity and a diameter of 240 nm. The inset image shows the electron diffraction pattern that is obtained at the center of the nanowire. The diffused pattern indicates that it is amorphous.

important because the crystallization completely changes the BMG mechanical properties which can be sustained in nanowires. Furthermore, the nanomechanical characteristics receive significant influence from surface effects, which are not negligible when the size reaches the nanoscale.[22] Evidently, the results of EDX in Figure 3 show that the peaks obtained from the Ar milled surface identify only Zr, Cu, and Al, which correspond to the original BMG compositions. However, the fracture surface includes O in addition to the original, indicating significant surface oxidation. To identify the structural phases of nanowires, we employed the FIB technique and a vein texture was sliced for TEM observations. To avoid excessive milling of the nanowire, a $W(CO)_6$ gas was exposed to the surface and the side walls of the sample were milled to a thickness of ~0.1 μm, as depicted in Figure 4a. Figure 4b is the bright-field TEM image showing the cross section of the nanowire that has 240 nm in diameter. The defective feature on the top of the nanowire was caused by the Ga irradiation. The inset shows the electron diffraction pattern that is obtained from the center of the nanowire. The diffused pattern can be recognized; thus we conclude that there is no trace of the crystallization in the nanowire.

The electron diffraction result provides direct evidence of the amorphous states. This can be further supported by the estimation of a cooling rate. When the nanospherical drop, as seen in Figure 2d, is quenched from the melting temperature, T_m, to the glass transition temperature, T_g, in an environment temperature, T_∞, the heat conduction differential equation under the nonequilibrium condition is given by

$$\frac{dT}{dt} + \frac{hS}{c\sigma V}(T - T_\infty) = 0 \quad (1)$$

where h is the heat transfer coefficient, S is the surface area, c is the specific heat, σ is the density, and V is the volume of a sphere. When $t = 0$, $T = T_m$; thus we can obtain

$$\frac{T - T_\infty}{T_m - T_\infty} = \exp\left(-\frac{hS}{c\sigma V}t\right) \quad (2)$$

The temperature reduced from $T_m = 1273$ K to $T_g = 706$ K in the air at $T_\infty = 300$ K,[21,23] and the physical values of the Zr based BMG are substituted into eq 2.[24] One can find $t = \sim 3$ ms for the 80 nm diameter sphere, and the cooling rate $(T_m - T_g)/t$ is obtained as $\sim 2 \times 10^5$ K/s. Although this is still under estimation because the thermal radiation is not taken into account, cooling at the current status is an extremely fast event to pass through the supercooled liquid region, which can be compared with the critical cooling rate of 1−10 K/s for a typical ingot of Zr based BMGs.[11,12]

On the fracture surface, there are not only the nanowires but also the round ridges that configure vein patterns, as seen in Figure 2a. To understand structural consequences of the

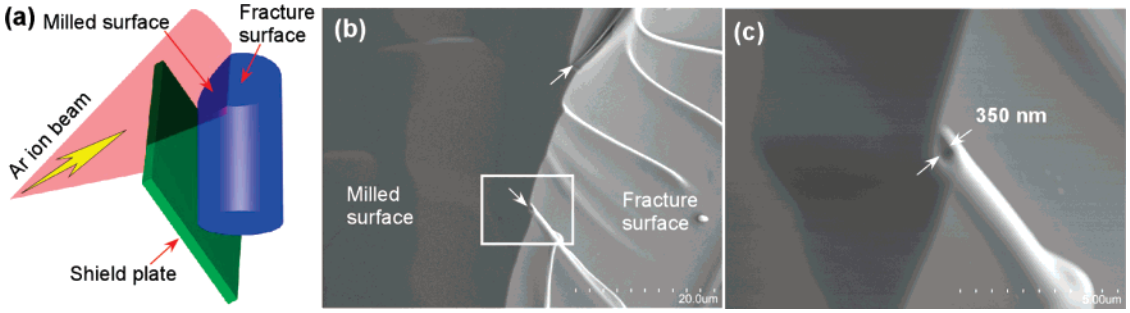

Figure 5. (a) Schematic diagram of the tilt Ar ion milling method. The Ti shield plate (green) located in front of the fractured sample (blue). The oblique sectional surface was prepared by removing the uncovered area of the shield with Ar ion irradiation (pink). (b) The SEM image represents the boundary between the milled surface (left) and the fracture surface (right). The white arrows indicate the nanotube locations. (c) Higher magnification SEM image of the nanotube was obtained from the white box in (b). The nanotube has an inner diameter of 350 nm.

ridges, we used the Ar ion milling to prepare an oblique sectional surface, as illustrated in Figure 5a. Figure 5b is the SEM image showing both the milled and fractured surfaces. For the left side of the image, the milled surface is featureless, and the EDX result in Figure 3 obtained from this area represents the bulk chemical components of the BMG. For the right side, the prior vein features can be recognized. Remarkably, at the boundary between the milled and fractured surfaces, the ridges labeled by the white arrows have a tubular structure. Figure 5c is the expanded image of the white box in Figure 5b. It shows that the inner diameter is 350 nm. Although the cylindrical feature is not a perfect round shape, the image provides the existence of the nanotube on the fracture surface.

Our studies demonstrate that the disordered atomic configuration of BMGs can be sustained in the nanostructures that were produced during the fracture processes. The high fraction of surface atoms on the nanowires does not cause crystallization. These findings provide important implications in understanding the structural stability of BMGs and broadening our knowledge in nanostructural configurations. Moreover, our experiments support the recent theoretical studies showing that a disordered structure is more favorable for metallic nanowires under stresses and strains.[8−10] The preferred disordered structure indicates that the metallic glass nanowires possess better structural stability under mechanical loading than the crystalline ones. In this study, we could not rule out surface oxidation and have not measured actual mechanical properties for individual nanowires. In both cases, further investigations such as the environmental dependence (for example, in air, in vacuum, or in noble gases) during nanostructure productions must be required to eliminate surface effects.

Acknowledgment. This work was supported by a Grant-In-Aid for Science Research on a Priority Areas "Research and Development Project on Advanced Metallic Glasses, Inorganic Materials and Joining Technology" and "Materials Science of Bulk Metallic Glasses" of the Ministry of Education, Culture, Sports, and Science, Japan.

References

(1) Craighead, H. G. *Science* **2000**, *290*, 1532.
(2) Iijima, S. *Nature* **1991**, *354*, 56.
(3) Morales, A. M.; Lieber, C. M. *Science* **1998**, *279*, 208.
(4) Kondo, Y.; Takayanagi, K. *Science* **2000**, *289*, 606.
(5) Huang, Y.; Duan, X.; Cui, Y.; Lieber, C. M. *Nano Lett.* **2002**, *2*, 101.
(6) (a) Yuan, X. Y.; Wu, G. S.; Xie, T.; Lin, Y.; Zhang, L. D. *Nanotechnology* **2004**, *15*, 59. (b) Xue, D.; Shi, H. *Nanotechnology* **2004**, *15*, 1752. Both show short arrays of amorphous nanowires that were created by electron deposition methods.
(7) Xu, S.; Tian, M.; Wang, J.; Xu, J.; Redwing, J. M.; Chen, M. H. W. *Small* **2005**, *12*, 1221 discussed the local amorphization on metallic nanowires induced by electron irradiations.
(8) Wang, D.; Zhao, J.; Hu, S.; Yin, X.; Liang, S.; Liu, Y.; Deng, S. *Nano Lett.* **2007**, *7*, 1208.
(9) Ikeda, H.; Qi, Y.; Çagin, T.; Samwer, K.; Johnson, W. L.; Goddard, W. A., III. *Phys. Rev. Lett.* **1999**, *82*, 2900.
(10) Koh, S. J. A.; Lee, H. P.; Lu, C.; Cheng, Q. H. *Phys. Rev. B* **2005**, *72*, 085414.
(11) Greer, A. L. *Science* **1995**, *267*, 1947.
(12) Inoue, A. *Acta. Mater.* **2000**, *48*, 279.
(13) Greer, A. L.; Ma, E. *MRS Bull.* **2007**, *32*, 611.
(14) Wang, G.; Zhao, D. Q.; Bai, H. Y.; Pan, M. X.; Xia, A. L.; Han, B. S.; Xi, X. K.; Wu, Y.; Wang, W. H. *Phys. Rev. Lett.* **2007**, *98*, 235501.
(15) Chen, M.; Inoue, A.; Zhang, W.; Sakurai, *Phys. Rev. Lett.* **2006**, *96*, 245502.
(16) Hays, C. C.; Kim, C. P.; Johnson, W. L. *Phys. Rev. Lett.* **2000**, *84*, 2901.
(17) Pampillo, C. A. *J. Mater. Sci.* **1975**, *10*, 1194.
(18) Spaepen, F. *Acta. Mater.* **1975,** *23*, 615.
(19) Bengus, V. Z.; Tabachnikova, E. D.; Miškuf, J.; Csach, K.; Ocelík, V.; Johnson, W. L.; Molokanov, V. V. *J. Mater. Sci.* **2000**, *35*, 4449.
(20) Lewandowski, J. J.; Greer, A. L. *Nature Mater.* **2006**, **5**, 15.
(21) Yokoyama, Y.; Akeno, Y.; Yamasaki, T.; Liaw, P. K.; Buchanan, R. A.; Inoue, A. *Mater. Trans.* **2005**, *46*, 2755.
(22) Nakayama, K. S.; Yokoyama, Y.; Sakurai, T.; Inoue, A. *Appl. Phys. Lett.* **2007**, *90*, 183105.
(23) Yokoyama, Y.; Inoue, H.; Fukaura, K.; Inoue, *Mater. Trans.* **2002**, *43*, 575.
(24) We used the following values from refs 21, 25, and 26; $h = 10$ $W{\cdot}m^{-2}{\cdot}K^{-1}$, $c = 372$ $J{\cdot}Kg^{-1}{\cdot}K^{-1}$, and $\sigma = 6.825 \times 10^3$ $Kg{\cdot}m^{-3}$.
(25) Katayama, K., Ed. *Data Book: Heat Transfer*, 4th ed.; The Japan Society of Mechanical Engineers: Tokyo, 1986; pp 69 and 329.
(26) Waseda, Y.; Shibata, H.; Ohta, H. Thermal properties of bulk Glassy alloys. In *Proceeding of the Sohn International Symposium on Thermo and Physicochemical Principles: Nonferrous High Temperature Processing*; Kongoli, F., Reddy, R. G., Eds.; The Minerals, Metals & Materials Society: San Diego, CA, 2006; pp 649−658.

NL0727462